



# Interfacial charge transfer induced dual-active-sites of heterostructured $\text{Cu}_{0.8}\text{Ni}_{0.2}\text{WO}_4$ nanoparticles in ammonia borane methanolysis for fast hydrogen production

Jinyun Liao<sup>a,b,1</sup>, Youxiang Shao<sup>a,1</sup>, Yufa Feng<sup>a</sup>, Jing Zhang<sup>a</sup>, Chunxia Song<sup>a</sup>, Wei Zeng<sup>a</sup>, Jinting Tang<sup>a</sup>, Huafeng Dong<sup>c</sup>, Quanbing Liu<sup>b,\*</sup>, Hao Li<sup>a,\*</sup>

<sup>a</sup> School of Chemistry and Materials Engineering, Guangdong Provincial Key Laboratory for Electronic Functional Materials and Devices, Huizhou University, Huizhou 516007, China

<sup>b</sup> Guangzhou Key Laboratory of Clean Transportation Energy Chemistry, School of Chemical Engineering and Light Industry, Guangdong University of Technology, Guangzhou 510006, China

<sup>c</sup> School of Physics and Optoelectronic Engineering, Guangdong University of Technology, Guangzhou 510006, China

## ARTICLE INFO

### Keywords:

Methanolysis  
Ammonia borane dehydrogenation  
Heterogeneous catalysis  
Heterojunction  
Electronic structure

## ABSTRACT

Ammonia borane (AB) methanolysis can be applied as an integrated technology for the storage and production of hydrogen with high efficiency and safety. However, the commercial applications of AB methanolysis are restricted by the high costs of noble metal-based catalysts. In this study, a series of cheap  $\text{Cu}_x\text{Ni}_{1-x}\text{WO}_4$  ( $x = 0, 0.2, 0.4, 0.6, 0.8$  and  $1$ ) catalysts have been designed for AB methanolysis. Among them, heterostructured  $\text{Cu}_{0.8}\text{Ni}_{0.2}\text{WO}_4$  exhibits the highest turnover frequency (TOF) of  $59.0 \text{ mol}_{\text{hydrogen}} \text{ min}^{-1} \text{ mol}_{\text{cat}}^{-1}$ , which is among the most active noble metal-free catalysts. The catalytic activity of the catalysts is well maintained after eight catalytic cycles. It is experimentally and theoretically demonstrated that electron transfer occurs on the  $\text{CuWO}_4/\text{NiWO}_4$  interface in  $\text{Cu}_{0.8}\text{Ni}_{0.2}\text{WO}_4$  nanoparticles, leading to the formation of dual active sites on the surface of heterostructured  $\text{Cu}_{0.8}\text{Ni}_{0.2}\text{WO}_4$ . More importantly, it is discovered that the dual active sites, namely, Cu and Ni sites, account for the adsorption and activation of AB and  $\text{CH}_3\text{OH}$ , respectively, which can cooperate together to boost the catalytic activity in a significant way. The plausible mechanism for AB methanolysis has also been proposed and the scission of O-H bond is identified to be the rate-determining step. The findings in this study could serve as guidance for the creation of novel catalysts with excellent performance and low cost in AB methanolysis.

## 1. Introduction

Hydrogen has been regarded as a green energy carrier with the merits of high gravimetric energy density and zero emissions, receiving extensive attention over the past decade [1,2]. One of the most important applications of hydrogen is as fuel in the hydrogen-oxygen fuel cells, which can serve as power source systems in devices including portable electronic devices, spacecrafts, and vehicles. Nevertheless, the high-efficiency and safe storage and transportation of hydrogen have remained a major challenge, deemed as a bottleneck of the large-scale applications of hydrogen [3]. To fix this problem, many researchers have made great efforts and several strategies have been put forward

[4–6]. Among them, the storage and transportation of hydrogen in the form of chemical hydrides is believed to be a promising route due to the high efficiency and safety of the process. Ammonia borane (AB) is a representative chemical hydride with a high hydrogen content of 19.6 wt% that can be applied to produce hydrogen by hydrolysis and methanolysis. Compared to AB hydrolysis, AB methanolysis has several benefits [7]. First, ammonia gas, which is unfavorable in a hydrogen-oxygen fuel cell, will not be produced during the process of AB methanolysis. Second,  $\text{NH}_4\text{B}(\text{OCH}_3)_4$  generated during AB methanolysis can be easily converted back to AB at room temperature by chemical reaction, which makes AB renewable and can remarkably lower the overall cost of this technology. Third, thanks to the low freezing point of

\* Corresponding authors.

E-mail addresses: [liuqb@gdut.edu.cn](mailto:liuqb@gdut.edu.cn) (Q. Liu), [lihao180@126.com](mailto:lihao180@126.com) (H. Li).

<sup>1</sup> Both authors contribute equally to this work.

methanol (lower than  $-90\text{ }^{\circ}\text{C}$ ), AB methanolysis technology can be applied to produce hydrogen at very low temperatures, which is of extreme importance in cold areas. Over the past ten years, AB hydrolysis for the hydrogen production catalyzed by various catalysts has been extensively investigated by many groups, and significant progress has been made on the catalyst design, reaction kinetics, and reaction mechanisms [8–12]. In contrast, AB methanolysis has been seldom concerned and several important issues in this field need to be well addressed. It is widely acknowledged that the development of inexpensive and robust catalysts is one of the key issues for the industrial applications of AB methanolysis [7]. Although noble metal-based catalysts show high catalytic performance in AB methanolysis, their high costs significantly limit their application as catalysts. Several types of noble metal-free catalysts, such as Co-based and Cu-based alloys [13, 14], oxide catalysts [15], and metal-oxide composites [16], have been developed, which are active in AB methanolysis. Unfortunately, their catalytic performance is still not satisfactory, and the development of new types of cheap catalysts with superior catalytic activity is in great need.

Recently, heterostructured nanoparticles have sparked increasing research interest in the area of catalysis due to their special compositions and structures [17,18]. Heterostructured nanoparticles are composed of multiple condensed nanoscale domains with different material compositions, which were connected to each other through interfaces. In contrast to homogeneous nanoparticles, heterostructured nanoparticles often display robust reactivity in view of the synergistic effects among individual components and/or new properties caused by the integrated structures. Compared to the traditional heterojunction composed of distinct layers, heterostructured nanoparticles possess rich phase interfaces, on which there may be plentiful active sites for the catalysis. In the field of AB dehydrogenation for hydrogen production, several groups have evidenced that heterostructured nanoparticles show improved catalytic activity, such as Cu/Co(OH)<sub>2</sub> [19], NiO/Ni [20], Ni/Ni<sub>2</sub>P [21], CoP-CoO [22], and Cu/Cu<sub>0.76</sub>Co<sub>0.24</sub>O<sub>4</sub> [23]. Notably, most of these heterostructured catalysts are composed of metals, metal oxides, metal hydroxides, and metal phosphides, whereas other type of heterostructured nanoparticles for AB dehydrogenation has been seldom reported. Besides, most of these studies deal with AB hydrolysis instead of AB methanolysis. It is well known that AB methanolysis is much slower than AB hydrolysis. In addition, generally speaking, there are multiple active sites in the heterostructured nanoparticle catalysts for AB dehydrogenation. However, the detailed roles of different active sites, the synergistic effects among different active sites, and the impacts of electronic structures on the catalytic performance have not been well understood, yet. Thus, further investigations are indispensable for a better understanding of the catalytic behaviors of heterostructured nanoparticles in AB dehydrogenation.

Here, insoluble tungstates with different components (Cu<sub>x</sub>Ni<sub>1-x</sub>WO<sub>4</sub>,  $x = 0, 0.2, 0.4, 0.6, 0.8$  and  $1$ ) were designed and their catalytic behaviors in AB methanolysis were investigated systematically. As far as we know, this is the first example of the use of insoluble salts as catalysts for AB methanolysis. Notably, it has been well documented in the literature that CuWO<sub>4</sub> and NiWO<sub>4</sub> can be used in photocatalysts [24], electrocatalysts [25], and supercapacitors [26]. However, their utilization as heterogeneous catalysts in AB methanolysis has not yet been reported. Herein, it was discovered that heterostructured Cu<sub>x</sub>Ni<sub>1-x</sub>WO<sub>4</sub> nanoparticles with an optimized Cu/Ni ratio, namely Cu<sub>0.8</sub>Ni<sub>0.2</sub>WO<sub>4</sub>, exhibited robust catalytic activity in AB methanolysis with a turnover frequency (TOF) of  $59.0\text{ mol}_{\text{hydrogen}}\text{ min}^{-1}\text{ mol}_{\text{cat}}^{-1}$ . A survey of the literature indicates that our heterostructured Cu<sub>0.8</sub>Ni<sub>0.2</sub>WO<sub>4</sub> nanoparticles show higher catalytic activity than most non-noble-metal catalysts in AB methanolysis according to the TOF values. Meanwhile, it is demonstrated that electron transfer in the CuWO<sub>4</sub>/NiWO<sub>4</sub> interfaces in Cu<sub>x</sub>Ni<sub>1-x</sub>WO<sub>4</sub> plays a key role in boosting catalytic activity. More importantly, it was discovered that the dual active sites, viz. Cu and Ni sites in the heterostructured Cu<sub>x</sub>Ni<sub>1-x</sub>WO<sub>4</sub> nanoparticles were

responsible for the adsorption and activation of AB and CH<sub>3</sub>OH, respectively. The findings in this work may provide new insights into the design of novel heterostructured nanoparticle catalysts for AB methanolysis.

## 2. Experimental section

### 2.1. Catalyst preparation

The chemical reagents used were all analytical grade and obtained directly from the suppliers. To prepare the Cu<sub>x</sub>Ni<sub>1-x</sub>WO<sub>4</sub> nanoparticles,  $2x\text{ mmol Cu(NO}_3)_2\cdot 6\text{H}_2\text{O}$  and  $(2 - 2x)\text{ mmol Ni(NO}_3)_2\cdot 6\text{H}_2\text{O}$  were dissolved in 40 mL of water ( $x = 1, 0.8, 0.6, 0.4, 0.2$ , and  $0$ ). Subsequently, 6 mmol sodium salicylate was added under agitation. Sodium tungstate (2 mmol) was dissolved in 40 mL of water, which was then added slowly to the prepared Cu/Ni mixture solution. The resultant solution was poured into a Teflon-lined stainless autoclave and subjected to hydrothermal treatment at  $170\text{ }^{\circ}\text{C}$  for 6 h. Subsequently, the collected powder was resined and calcined at  $550\text{ }^{\circ}\text{C}$  for 3 h.

### 2.2. Characterization

X-ray diffraction (XRD) analysis was carried out on a Rigaku Ultima IV diffractometer with Cu K $\alpha$  radiation ( $\lambda = 1.5406\text{ \AA}$  at 40 kV and 40 mA). A FEI Tecnai G2 F20 S-TWIN transmission electron microscope was used to examine the crystal structures, particle size, and morphology. On a Kratos Axis Ultra DLD X-ray photoelectron spectrometer using Al K radiation, X-ray photoelectron spectroscopy (XPS) spectra were captured. Using a Micromeritics ASAP 2020 nitrogen adsorption analyzer, the samples' surface areas and nitrogen adsorption-desorption isotherms were determined. Inductively coupled plasma atomic emissions. To get the FTIR spectra of the samples, Fourier transform infrared (FTIR) spectroscopic examination was carried out using a Bruker Tensor 27 FTIR spectrometer. A Spectro Arcos FHS12 inductively coupled plasma atomic emission spectrometer (ICP-AES) was applied to determine the molar ratios of the various metals in the catalysts. Using a gas chromatograph (Agilent GC 7820A) outfitted with a 5A molecular sieve column and thermal conductive detector, the gas produced during AB methanolysis was identified.

### 2.3. Catalytic experiments

In a round-bottom flask that was sealed and attached to a glass burette, the catalytic methanolysis of AB was carried out. A water bath was used to keep the reaction temperature at  $25\text{ }^{\circ}\text{C}$  in an open environment. Typically, 10.0 mg of powdered catalyst was highly dispersed in 10 mL of supreme anhydrous methanol (Aladdin Reagent Co., Ltd., Shanghai, China, water content  $\leq 20\text{ ppm}$ ) under ultrasonication. The aforementioned solution was then swiftly mixed with 10.0 mL of a methanol solution containing 20.0 mmol of NaOH and 3.0 mmol of AB. Numerous bubbles started to appear as soon as AB came into contact with the catalyst, suggesting the production of hydrogen. Water displacement in a gas burette was recorded in order to calculate the volume of hydrogen. The stability and reusability tests were carried out according to the following process. After the previous run of AB methanolysis, the catalyst was collected, washed, and dried. Similar to the first run, the new catalytic run would begin and the hydrogen volume was recorded. This process was repeated eight times.

## 3. Results and discussion

### 3.1. Catalyst characterization

The XRD patterns of a series of Cu<sub>x</sub>Ni<sub>1-x</sub>WO<sub>4</sub> samples are shown in Fig. 1. The XRD patterns of CuWO<sub>4</sub> and NiWO<sub>4</sub> match well with the standard XRD patterns of CuWO<sub>4</sub> in the triclinic phase (PDF#880269)

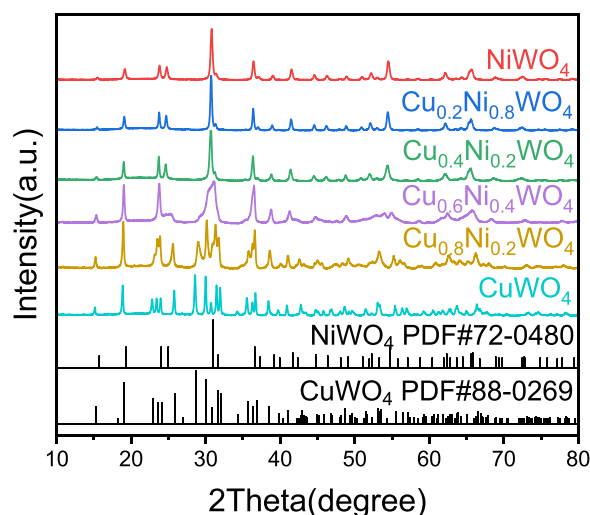


Fig. 1. XRD patterns of the  $\text{Cu}_x\text{Ni}_{1-x}\text{WO}_4$  samples.

and  $\text{NiWO}_4$  in the monoclinic phase (PDF#720480), respectively. As for the other four samples, those samples display the characteristic peaks of both  $\text{CuWO}_4$  and  $\text{NiWO}_4$ , implying that  $\text{CuWO}_4$  and  $\text{NiWO}_4$  may be combined in the form of composites in these samples. No peaks related to the impurity, such as  $\text{WO}_3$ ,  $\text{CuO}$  or  $\text{NiO}$ , were found, indicating that there were no single oxides in the samples. ICP-AES analysis was performed on different  $\text{Cu}_x\text{Ni}_{1-x}\text{WO}_4$  samples, and the results are displayed in Table S1 in the Supplementary materials. As can be observed, the atomic ratio of Cu to Ni to W is close to the designed values, implying that the molar ratios of Cu to Ni in the obtained tungstate composites could be finely controlled by tuning the amounts of starting materials in the synthesis.

The sizes and morphology of the different  $\text{Cu}_x\text{Ni}_{1-x}\text{WO}_4$  samples were examined by transmission electron microscopy (TEM), and the results are shown in Fig. 2. All six samples were nanoparticles with average sizes in the range of 20–100 nm. Average particle sizes of approximately 100, 60, and 20 nm were observed for  $\text{CuWO}_4$ ,  $\text{Cu}_{0.8}\text{Ni}_{0.2}\text{WO}_4$ , and  $\text{Cu}_{0.6}\text{Ni}_{0.4}\text{WO}_4$  (Fig. 2a–c);  $\text{Cu}_{0.4}\text{Ni}_{0.6}\text{WO}_4$  and  $\text{Cu}_{0.2}\text{Ni}_{0.8}\text{WO}_4$  (Fig. 2d and e); and  $\text{NiWO}_4$  nanoparticles (Fig. 2f), respectively. Interestingly, the average particle size decreased as Ni content increased. To further clarify the crystal structures of  $\text{Cu}_{0.8}\text{Ni}_{0.2}\text{WO}_4$ , the sample was analyzed using high-resolution TEM (HRTEM). The lattice spacings of ca. 0.36 nm (Fig. 2g and h) can be attributed to the distance of the (110) plane of  $\text{NiWO}_4$  in the monoclinic phase, respectively. In addition, the lattice spacings of ca. 0.22, 0.30, 0.21, 0.47, and 0.28 nm can be ascribed to the distance of the  $(-102)$ ,  $(1-11)$ ,  $(-1-21)$ ,  $(100)$ , and  $(111)$  planes of  $\text{CuWO}_4$  in the triclinic phase, respectively. Notably, HRTEM images indicated distinct interfaces between  $\text{CuWO}_4$  and  $\text{NiWO}_4$  nanocrystals (marked with dotted lines), suggesting that the  $\text{Cu}_{0.8}\text{Ni}_{0.2}\text{WO}_4$  nanoparticles were composed of  $\text{CuWO}_4$  and  $\text{NiWO}_4$  nanocrystals and that Cu and Ni atoms were not uniformly mixed at the atomic level.

The FTIR spectra of the  $\text{Cu}_x\text{Ni}_{1-x}\text{WO}_4$  samples were shown in Fig. 3a. All the samples showed absorption peaks at around 3420 and 1630  $\text{cm}^{-1}$ , which could be attributed to the symmetrical/antisymmetrical stretching vibration of  $\text{H}_2\text{O}$  molecule adsorbed on the catalyst surface and the HO–H bending vibration, respectively [27]. As for  $\text{CuWO}_4$ , three characteristic peaks were found at around 909, 551, and 466  $\text{cm}^{-1}$ . The first peak corresponded to the stretching vibration of  $\text{W}=\text{O}$  in the octahedron of  $\text{WO}_3$ , while the other two can be ascribed to the stretching vibrations of Cu–O, confirming the formation of  $\text{CuWO}_4$  [26]. As for  $\text{NiWO}_4$ , the peaks at around 876 and 822  $\text{cm}^{-1}$  can be attributed to the vibration of the  $\text{WO}_2$  entity present in the  $\text{W}_2\text{O}_8$  groups. The peaks at 698 and 612  $\text{cm}^{-1}$  are typical of a two-oxygen bridge

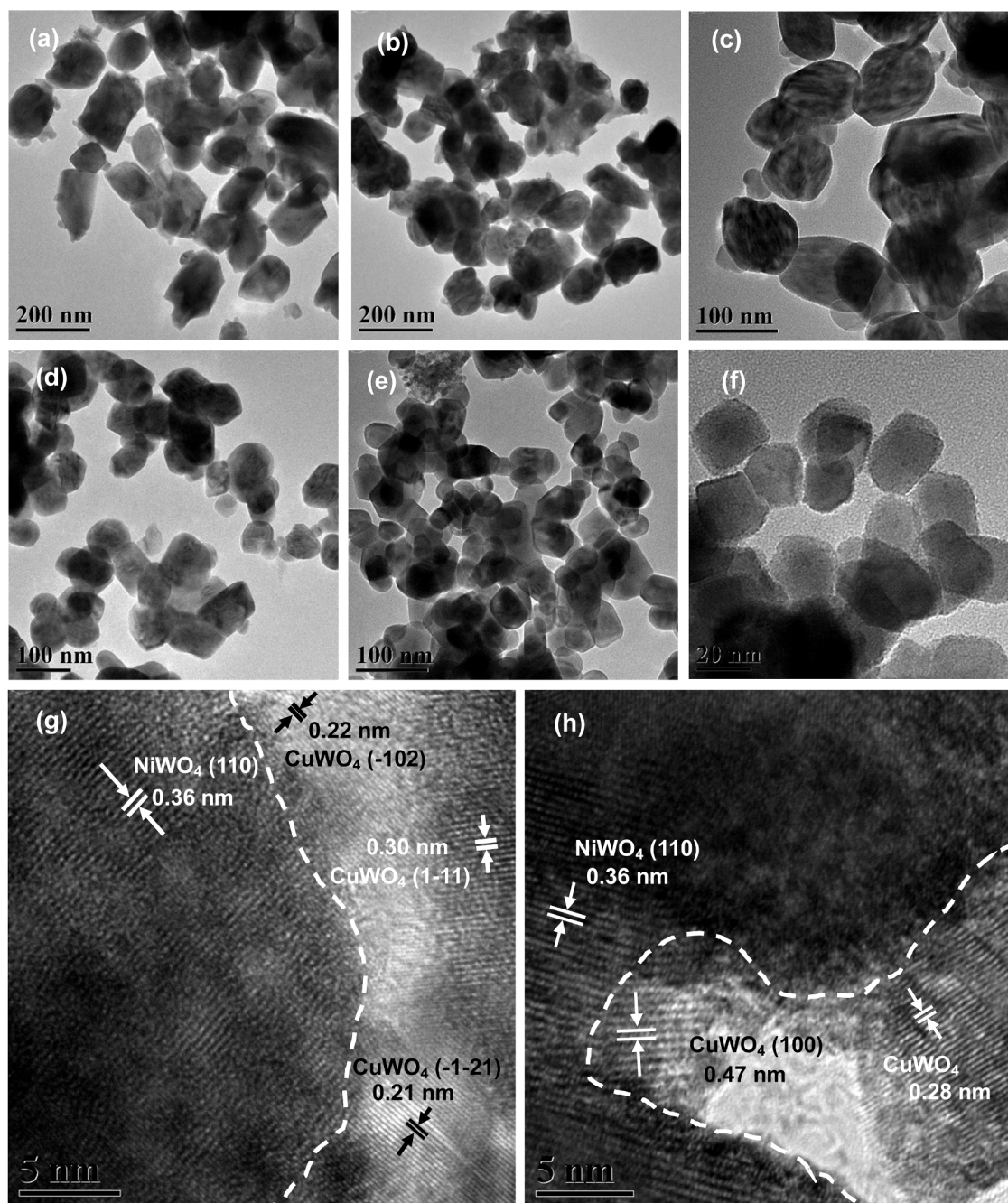
( $\text{W}_2\text{O}_2$ ). Absorption below 500  $\text{cm}^{-1}$  can be associated with the asymmetric stretching vibrations of the  $\text{NiO}_6$  polyhedra. These peaks match well with those of  $\text{NiWO}_4$  reported in the literature [28]. As for the  $\text{Cu}_x\text{Ni}_{1-x}\text{WO}_4$  composite samples, the characteristic peaks of both  $\text{CuWO}_4$  and  $\text{NiWO}_4$  still exist. The  $\text{Cu}_x\text{Ni}_{1-x}\text{WO}_4$  nanoparticles were analyzed by XPS in order to know the chemical states and the electronic structures present in the samples. In the XPS spectrum of  $\text{CuWO}_4$  (Fig. 3b), besides the two satellites (noted as Sat.), there are two peaks centered at 934.6 and 954.3 eV, corresponding to  $\text{Cu}^{2+}$  of  $\text{CuWO}_4$  [29]. Interestingly, as the Ni content increased, the characteristic peaks of  $\text{Cu}^{2+}$  shifted negatively. For example, the  $\text{Cu } 2p_{3/2}$  and  $\text{Cu } 2p_{1/2}$  peaks of  $\text{Cu}_{0.8}\text{Ni}_{0.2}\text{WO}_4$  were respectively centered at 934.3 and 953.1 eV, which were 0.3 and 0.2 eV lower than those of  $\text{CuWO}_4$ . In the XPS spectrum of  $\text{NiWO}_4$  (Fig. 3c), the characteristic peaks of  $\text{Ni } 2p_{3/2}$  and  $\text{Ni } 2p_{1/2}$  were located at 855.2 and 872.8 eV, respectively, which matched well with the value for  $\text{Ni}^{2+}$  of  $\text{NiWO}_4$  reported in the literature [30]. When Cu was incorporated into the samples, the characteristic  $\text{Ni}^{2+}$  peaks shifted positively. For example, the binding energies of  $\text{Ni}^{2+}$  in  $\text{Cu}_{0.8}\text{Ni}_{0.2}\text{WO}_4$  were respectively 856.0 and 873.7 eV, which were 0.8 and 0.9 eV higher than those of  $\text{Ni}^{2+}$  of  $\text{NiWO}_4$ . Considering the XPS results of Cu 2p and Ni 2p, it is clear that electron transfer occurred between  $\text{Ni}^{2+}$  and  $\text{Cu}^{2+}$  when  $\text{Cu}_x\text{Ni}_{1-x}\text{WO}_4$  was formed. The electrons migrated from  $\text{Ni}^{2+}$  to  $\text{Cu}^{2+}$ , resulting in positive and negative shifts of the  $\text{Ni}^{2+}$  and  $\text{Cu}^{2+}$  peaks, respectively, in the XPS spectra. Regarding the XPS spectra of W 4f for  $\text{Cu}_x\text{Ni}_{1-x}\text{WO}_4$  (Fig. 3d), it was noted that the W 4f peaks were initially negatively shifted and then positively shifted as the increment of Cu contents. That is, the W 4f peaks of all the  $\text{Cu}_x\text{Ni}_{1-x}\text{WO}_4$  composite samples shifted to lower binding energies compared with the single component of  $\text{NiWO}_4$  and  $\text{CuWO}_4$ . This observation implies that some electrons migrated from  $\text{Ni}^{2+}$  to  $\text{W}^{6+}$  in the  $\text{Cu}_x\text{Ni}_{1-x}\text{WO}_4$  composites.

Fig. S1a in the Supplementary materials displays the  $\text{N}_2$  adsorption–desorption isotherms of the  $\text{Cu}_x\text{Ni}_{1-x}\text{WO}_4$  samples. The adsorption–desorption isotherms of  $\text{CuWO}_4$  reveal an unclosed curve with a low BET surface area of 3.8  $\text{m}^2 \text{g}^{-1}$ . According to the literature, when a sample possesses ink-bottle pores, its adsorption–desorption isotherm is always unclosed [31]. In that case, the adsorption of  $\text{N}_2$  is much easier than the desorption, resulting in unclosed adsorption–desorption isotherms. Except  $\text{CuWO}_4$ , the other five samples had typical hysteresis loops in the high-pressure region, exhibiting type IV isotherms, which confirmed the mesoporous structure of the materials [32]. Notably, the BET surface areas increased with increasing Ni content, which resulted from decreased particle sizes (Fig. 2). Fig. S1b shows the pore size distribution of different samples, indicating that all of the  $\text{Cu}_x\text{Ni}_{1-x}\text{WO}_4$  samples had mesopores with a typical size of around 5 nm and further confirming the findings shown in Fig. S1a.

### 3.2. Catalytic performance and reaction kinetics

The catalytic activity of different  $\text{Cu}_x\text{Ni}_{1-x}\text{WO}_4$  samples in AB methanolysis for hydrogen production was also investigated. Considering that commercial methanol always contains some water, hydrogen could also be produced by AB hydrolysis but whether the hydrogen production could be attributed to methanolysis or hydrolysis would need to be investigated. In this work, the methanol used in the catalytic experiments was of supreme anhydrous grade ( $\text{H}_2\text{O}$  content  $\leq 20$  ppm). If all the water in the methanol participated in hydrolysis for hydrogen generation, it would only contribute to less than 1% of the total hydrogen present. Thus, the impact of AB hydrolysis in this study is negligible. When  $\text{Cu}_x\text{Ni}_{1-x}\text{WO}_4$  acts as catalysts, hydrogen release from methanol solution was depicted in Fig. 4a. Note that no hydrogen would be released without any catalysts, suggesting that the self-methanolysis of AB could not occur in the absence of proper catalysts. As shown in Fig. 4a, no hydrogen was generated in the presence of  $\text{NiWO}_4$ , verifying that  $\text{NiWO}_4$  itself could not catalyze AB methanolysis. As the Cu content in the  $\text{Cu}_x\text{Ni}_{1-x}\text{WO}_4$  samples increased, the catalysts exhibited improved





**Fig. 2.** TEM images of  $\text{CuWO}_4$  (a),  $\text{Cu}_{0.8}\text{Ni}_{0.2}\text{WO}_4$  (b),  $\text{Cu}_{0.6}\text{Ni}_{0.4}\text{WO}_4$  (c),  $\text{Cu}_{0.4}\text{Ni}_{0.6}\text{WO}_4$  (d),  $\text{Cu}_{0.2}\text{Ni}_{0.8}\text{WO}_4$  (e) and  $\text{NiWO}_4$  (f), and HRTEM images of  $\text{Cu}_{0.8}\text{Ni}_{0.2}\text{WO}_4$  (g, h).

catalytic activity. When  $\text{Cu}_{0.8}\text{Ni}_{0.2}\text{WO}_4$  acted as a catalyst, 42.5 mL of hydrogen could be produced within one minute and 201 mL of hydrogen would be released at the end of the reaction, corresponding to the complete methanolysis of AB. For comparison, the theoretical hydrogen volume is marked with a green dotted line. To clarify the active components in the catalysts, the catalytic activity of  $\text{WO}_3$  and  $\text{ZnWO}_4$  in AB methanolysis was also tested for references and no hydrogen was generated. This implied that W was inactive to AB methanolysis and the catalytic activity of the catalyst resulted from Cu and Ni. To identify the gas produced during AB methanolysis in the presence of  $\text{Cu}_{0.8}\text{Ni}_{0.2}\text{WO}_4$  as a catalyst, we analyzed the gas with GC and found there was only hydrogen, besides nitrogen and oxygen (Fig. S2). The nitrogen and oxygen came from the air, which were mixed into the hydrogen during GC analysis, verifying the high purity of the collected gas. For the sake of

activity comparison, TOF values of different samples are calculated (Fig. 4b). The detailed calculation can be found in Illustration S1 in the Supplementary materials. Except  $\text{NiWO}_4$ , the other five samples demonstrated catalytic activity in AB methanolysis. The TOF values of  $\text{Cu}_{0.2}\text{Ni}_{0.8}\text{WO}_4$ ,  $\text{Cu}_{0.4}\text{Ni}_{0.6}\text{WO}_4$ ,  $\text{Cu}_{0.6}\text{Ni}_{0.4}\text{WO}_4$ ,  $\text{Cu}_{0.8}\text{Ni}_{0.2}\text{WO}_4$ , and  $\text{CuWO}_4$  were 7.6, 8.3, 27.7, 59.0, and  $14.5 \text{ mol}_{\text{H}_2} \text{ min}^{-1} \text{ mol}_{\text{cat}}^{-1}$ , respectively. Different from  $\text{NiWO}_4$ ,  $\text{CuWO}_4$  can catalyze AB methanolysis with the TOF of  $14.5 \text{ mol}_{\text{H}_2} \text{ min}^{-1} \text{ mol}_{\text{cat}}^{-1}$ , which is not outstanding compared to those of catalysts recently reported in the literature [7]. When a small amount of Ni was incorporated into the  $\text{CuWO}_4$  sample, the activity of the resultant catalyst,  $\text{Cu}_{0.8}\text{Ni}_{0.2}\text{WO}_4$ , was remarkably enhanced with a TOF of  $59.0 \text{ mol}_{\text{H}_2} \text{ min}^{-1} \text{ mol}_{\text{cat}}^{-1}$ . When the content of Ni in the  $\text{Cu}_x\text{Ni}_{1-x}\text{WO}_4$  catalysts increased further, a pronounced drop in activity of the obtained catalysts was found. For



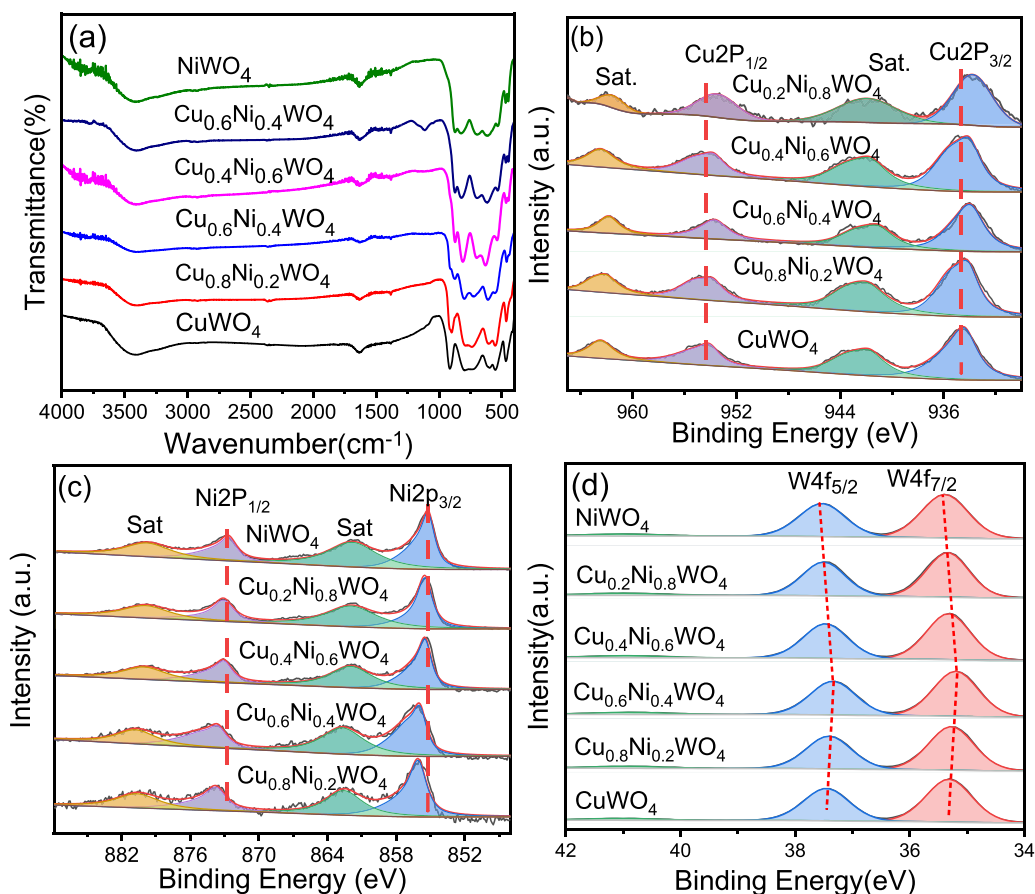


Fig. 3. FTIR spectra of  $\text{Cu}_x\text{Ni}_{1-x}\text{WO}_4$  samples (a), and XPS spectra of  $\text{Cu}_x\text{Ni}_{1-x}\text{WO}_4$  in Cu 2p (b), Ni 2p (c) and W 4f (d) regions.

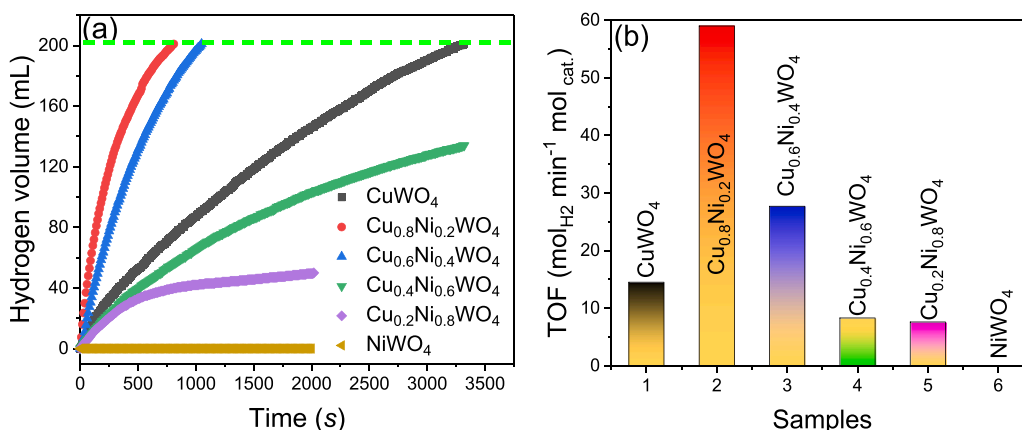


Fig. 4. Hydrogen release at different reaction time in the presence of  $\text{Cu}_x\text{Ni}_{1-x}\text{WO}_4$  samples (a) and the corresponding TOF (b).

example,  $\text{Cu}_{0.2}\text{Ni}_{0.8}\text{WO}_4$  showed relatively low catalytic activity, with a TOF of  $7.6 \text{ mol}_{\text{H}_2} \text{ min}^{-1} \text{ mol}_{\text{cat}}^{-1}$ . As mentioned above, the BET surface areas increased with increasing Ni content (Fig. S1a). Even though it had a relatively large BET surface area,  $\text{Cu}_{0.2}\text{Ni}_{0.8}\text{WO}_4$  possessed low catalytic activity, confirming that the Cu/Ni ratios rather than the BET surface areas of  $\text{Cu}_x\text{Ni}_{1-x}\text{WO}_4$  samples played a vital role in affecting their activity. For comparison, we also tested the catalytic activity of the  $\text{CuWO}_4/\text{NiWO}_4$  mixture with Cu/Ni ratio of 4:1 under the same reaction conditions. Evidently,  $\text{Cu}_{0.8}\text{Ni}_{0.2}\text{WO}_4$  shows much higher catalytic activity than  $\text{CuWO}_4/\text{NiWO}_4$  mixtures in AB methanolysis (Fig. S3), hinting a strong interaction between  $\text{CuWO}_4$  and  $\text{NiWO}_4$  in the heterostructured  $\text{Cu}_{0.8}\text{Ni}_{0.2}\text{WO}_4$  catalyst. In addition, to illustrate the role of

NaOH, we have added the hydrogen release results in the presence of NaOH (Fig. S4), verifying that the hydrogen production is enhanced by the addition of NaOH. According to Fu et al., NaOH can facilitate the activation of reactants and thus improve the hydrogen release from AB solution [33]. Can NaOH react with methanol to produce sodium methoxide and water? This issue should be addressed because the produced water may affect the hydrogen release. Based on the thermodynamic data and previous reports, it is concluded that this reaction will not happen under our reaction conditions (Please see Illustration S2 in Supplementary materials).

To compare the catalytic activity of the state-of-the-art catalysts with our  $\text{Cu}_{0.8}\text{Ni}_{0.2}\text{WO}_4$  catalyst, the TOF values of different catalysts are

shown in Table 1. As can be seen, our  $\text{Cu}_{0.8}\text{Ni}_{0.2}\text{WO}_4$  nanoparticles demonstrated robust catalytic activity towards AB methanolysis in terms of high TOF. Notably, it has been evidenced in the literature that the TOF of some inexpensive catalysts in the hydrolysis of AB can reach more than  $100 \text{ mol}_{\text{H}_2} \text{ min}^{-1} \text{ mol}_{\text{cat}}^{-1}$  [11,40–42]. As far as we know, among the noble metal-free catalysts, the  $\text{CoNi}/\alpha\text{-MoC}$  catalysts show the highest activity in AB hydrolysis with TOF of  $321.1 \text{ mol}_{\text{H}_2} \text{ min}^{-1} \text{ mol}_{\text{cat}}^{-1}$  [11]. In contrast, the methanolysis kinetics of AB is much more sluggish than that of AB hydrolysis, as shown in Table 1.

The reusability and the stability of the  $\text{Cu}_{0.8}\text{Ni}_{0.2}\text{WO}_4$  catalyst were verified by repeating the catalytic experiments eight times. Hydrogen evolution vs. reaction time in each catalytic run was recorded. The hydrogen production rate only decreased slightly as the cycle number increased (Fig. S5a). On the other hand, the volume of hydrogen could still reach 201 mL after the 8th run, indicative of a thorough methanolysis of AB. Both the characteristic peaks of  $\text{CuWO}_4$  and  $\text{NiWO}_4$  were observed in the XRD pattern of the  $\text{Cu}_{0.8}\text{Ni}_{0.2}\text{WO}_4$  catalyst after eight catalytic runs (Fig. S5b), which is similar to the fresh  $\text{Cu}_{0.8}\text{Ni}_{0.2}\text{WO}_4$  catalyst. The SEM image of the used  $\text{Cu}_{0.8}\text{Ni}_{0.2}\text{WO}_4$  catalyst demonstrated that the size and morphology of the used catalysts remained nearly unchanged when compared with fresh catalysts (Fig. S5c). The TEM image in Fig. S5d further confirmed that the  $\text{Cu}_{0.8}\text{Ni}_{0.2}\text{WO}_4$  catalysts after catalysis are almost the same in size and morphology. The HRTEM images (Figs. S5e and S5f) prove the presence of heterostructures in the used catalyst sample. All these results indicated that our  $\text{Cu}_{0.8}\text{Ni}_{0.2}\text{WO}_4$  catalyst exhibited good reusability and relatively high stability. Considering that  $\text{Cu}^{2+}$  is a potential contaminant in water environment and Cu ions leaching maybe happen during the catalysis, the accumulated concentration of  $\text{Cu}^{2+}$  in the reaction solution after eight catalytic cycles is determined with ICP-AES. It is discovered that Cu ions leaching can be ignored and the concentration of  $\text{Cu}^{2+}$  is as low as  $0.03 \text{ mg L}^{-1}$ , which is significantly lower than the threshold value ( $1.3 \text{ mg L}^{-1}$ ) in drinking water set by World Health Organization [43]. Another issue that needed to be addressed was the real active species involved in the catalytic process in this study. In AB hydrolysis, it was verified that the oxide-based catalysts could be reduced by AB, leading to the formation of metals or alloys on the catalyst surface, which acted as real active species during hydrolysis [42,44,45]. According to Yu et al., the CuNi alloy showed robust catalytic activity towards AB methanolysis [14]. Nevertheless, it isn't clear whether  $\text{Cu}_{0.8}\text{Ni}_{0.2}\text{WO}_4$  or the possible CuNi alloy generated via the reduction of  $\text{Cu}_{0.8}\text{Ni}_{0.2}\text{WO}_4$  with AB was the active species. To ascertain this, we analyzed the  $\text{Cu}_{0.8}\text{Ni}_{0.2}\text{WO}_4$  sample after the eighth catalytic cycle by XPS. As can be seen in Fig. S5g and S5h, there were no pronounced shifts of the characteristic peaks of  $\text{Cu}^{2+}$  and  $\text{Ni}^{2+}$  after reaction. In addition, no new characteristic peaks related to  $\text{Cu(0)}$  or  $\text{Ni(0)}$  appeared. These observations indicated that no  $\text{Cu(0)}$ ,  $\text{Ni(0)}$ , or CuNi alloy was formed after the catalytic reaction. It is likely that AB in the methanol medium could not reduce  $\text{Cu}^{2+}$  or  $\text{Ni}^{2+}$  in  $\text{Cu}_{0.8}\text{Ni}_{0.2}\text{WO}_4$  to metallic or alloy states. Thus, it can be concluded that the real catalyst in this study was  $\text{Cu}_{0.8}\text{Ni}_{0.2}\text{WO}_4$  itself rather than the CuNi alloy.

**Table 1**  
Comparison of TOF of some representative noble-metal-free catalysts.

Catalysts	TOF ( $\text{mol}_{\text{H}_2} \text{ mol}_{\text{cat}}^{-1} \text{ min}^{-1}$ )	Ref.
$\text{Cu}/\text{Co(OH)}_2$	61.63	[19]
$\text{Cu}_{0.8}\text{Ni}_{0.2}\text{WO}_4$	59.0	This work
$\text{Cu(OH)}_2/\text{Fe(OH)}_3$	50.3	[34]
$\text{G-Cu}_{36}\text{Ni}_{64}$	49.1	[14]
$\text{Mo}_x\text{-Ni}_{0.8}\text{Cu}_{0.2}\text{O}$	46.9	[35]
PVP-stabilized $\text{Co}_{0.7}\text{Ni}_{0.3}$	35.3	[13]
$\text{Cu-Cu}_2\text{O-CuO/C}$	24.0	[16]
$\text{G-Cu/Ni-NiO}_x$	17.72	[36]
Bunch like-CuO NA/CF	13.3	[37]
PVP-stabilized Ni	12.1	[38]
Mesoporous CuO nanostructures	2.41	[39]

To study the reaction kinetics of AB methanolysis in the presence of  $\text{Cu}_{0.8}\text{Ni}_{0.2}\text{WO}_4$  as a catalyst, the effects of AB amount, the catalyst dosages, and the reaction temperatures on the hydrogen evolution behaviors were examined. Fig. 5a displays the accumulated volume of hydrogen generated during AB methanolysis at different reaction times. As shown, the hydrogen volume increased as the amount of AB used increased. However, the initial reaction rate ( $r$ ) was almost the same independent of the AB amount. The correlation of  $\ln r$  and  $\ln n_{\text{AB}}$  is depicted in Fig. 5b. Apparently, AB methanolysis obeyed zero-order kinetics relative to AB, according to a fitted line with a slope of 0.018. The hydrogen production rate was larger at a higher catalyst mass, as seen in Fig. 5c. The relationship of  $\ln r$  and  $\ln m$  (mass) is illustrated in Fig. 5d. In relation to the catalyst, AB methanolysis appeared to follow pseudo-first-order kinetics, as indicated by the fitted line's slope of 1.17. Fig. 5e shows the hydrogen evolution curves at different reaction temperatures ( $T$ ), indicating that higher reaction temperatures led to faster hydrogen production.  $\ln k$  (the rate constant) vs.  $1/T$  are plotted in Fig. 5f. When  $\text{Cu}_{0.8}\text{Ni}_{0.2}\text{WO}_4$  was used as a catalyst in this reaction, the activation energy was determined using the Arrhenius equation to be  $38.9 \text{ kJ mol}^{-1}$ .

Notably, the hydrogen release lines are not straight lines and there are two or more slopes in these lines in Fig. 5a, c and e. A divergence from the linear correlation of the accumulated hydrogen volume with reaction time at the late stage of the reaction was frequently seen in AB hydrolysis or methanolysis [35,46,47]. As the reaction of AB hydrolysis or methanolysis proceeds, the concentration of AB decreases, which will affect the reactant diffusion. Chen et al. attributed this deviation from the linear dependence to the external diffusion limitation of AB [47].

### 3.3. Identification of dual active sites and reaction mechanism

As discussed above, when  $\text{CuWO}_4$  and  $\text{NiWO}_4$  are combined, the transfer of electrons occurs at the  $\text{CuWO}_4/\text{NiWO}_4$  interface. To further confirm the charge separation and transfer on the  $\text{CuWO}_4/\text{NiWO}_4$  interfaces, we carried out density functional theory (DFT) calculations. The computational details can be seen in the Supplementary materials. Fig. 6a shows the electron density difference of the  $\text{CuWO}_4/\text{NiWO}_4$  interface. Clearly, numerous positive and negative charges are accumulated in the interface, hinting the charge separation between  $\text{CuWO}_4$  and  $\text{NiWO}_4$ , which conduces to the formation of active sites for the catalysis. To analyze their electronic structures, the density of states (DOS) of  $\text{CuWO}_4$ ,  $\text{NiWO}_4$ , as well as  $\text{Cu}_{0.8}\text{Ni}_{0.2}\text{WO}_4$  were shown in Fig. 6b–d. DOS of  $\text{CuWO}_4$  catalysts at Fermi level is close to zero, indicative of the poor ability of electron transfer in  $\text{CuWO}_4$ . In contrast, after  $\text{NiWO}_4$  is introduced, DOS of  $\text{Cu}_{0.8}\text{Ni}_{0.2}\text{WO}_4$  at Fermi level is not zero, indicative of the metallic nature of the interface, which is favorable for the electron transfer at the interface [48]. According to the data of DOS, the d band center ( $\epsilon_d$ ) of different catalysts can be figured out, which is deemed as an indicator for the binding strength of reactants on active sites. As can be seen in Fig. 6b and c,  $\epsilon_d\text{-Cu}$  is  $-1.78 \text{ eV}$  for  $\text{CuWO}_4$  while  $\epsilon_d\text{-Ni}$  is  $-2.03 \text{ eV}$  for  $\text{NiWO}_4$ . In contrast,  $\epsilon_d\text{-Cu}$  and  $\epsilon_d\text{-Ni}$  for  $\text{Cu}_{0.8}\text{Ni}_{0.2}\text{WO}_4$  become  $-1.45 \text{ eV}$  and  $-1.47 \text{ eV}$ , respectively. Evidently, both  $\epsilon_d\text{-Cu}$  and  $\epsilon_d\text{-Ni}$  upshift to the Fermi level when the heterostructured  $\text{Cu}_{0.8}\text{Ni}_{0.2}\text{WO}_4$  nanoparticles are formed. The d band theories claim that the higher d states in energy in relation to the Fermi level, the more empty antibonding orbitals, which are a sign of a stronger adsorption bond of reactants on active sites [49,50]. Thus, it is expectable that the adsorption of  $\text{CH}_3\text{OH}$  and AB on the  $\text{Cu}_{0.8}\text{Ni}_{0.2}\text{WO}_4$  catalysts will be enhanced compared to that of single  $\text{CuWO}_4$  and  $\text{NiWO}_4$ . To better understand the influence of charge transfer on AB methanolysis from the viewpoint of reaction mechanism, the adsorption behaviors of the reactants, namely  $\text{CH}_3\text{OH}$  and AB, on different catalyst surface were investigated. As shown in Fig. 7a and b, the  $E_{\text{ad}}$  (adsorption energy) of  $\text{CH}_3\text{OH}$  and AB on the  $\text{NiWO}_4$  is  $-1.60$  and  $-0.91 \text{ eV}$ , respectively. The corresponding structural simulations can be seen in Fig. S6a and S6b. The relatively low  $E_{\text{ad}}$  is indicative of weak adsorption

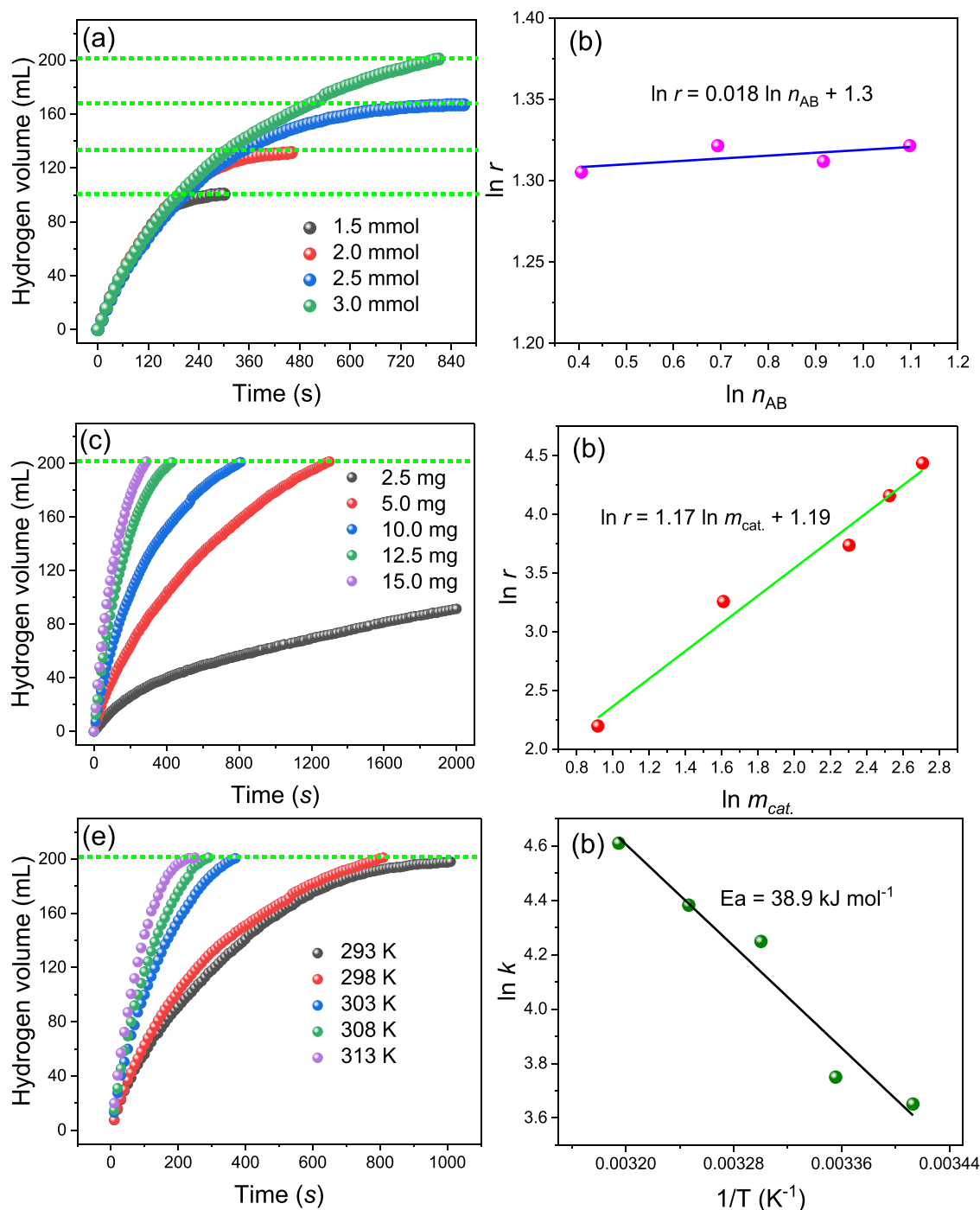


**Fig. 5.** Hydrogen releasing curves at different AB dosages (a); plot of  $\ln$  ( $H_2$  evolution rate) vs.  $\ln$  (AB amount) (b); Hydrogen releasing curves at different catalyst dosages (c); plot of  $\ln$  ( $H_2$  evolution rate) vs.  $\ln$  (catalyst weight) (d); hydrogen releasing curves at different reaction temperatures (e); plot of  $\ln k$  vs.  $1/T$  (f).

of the reactants on the  $NiWO_4$  catalyst surface, which is unfavorable for the activation of the reactants and the subsequent methanolysis reaction. This observation may account for the fact that  $NiWO_4$  is nearly inert in AB methanolysis. When  $CuWO_4$  is used as catalysts,  $E_{ad}$  of  $CH_3OH$  is slightly lower than that on  $NiWO_4$  surface ( $-1.50 \text{ eV}$  vs.  $-1.60 \text{ eV}$ ) but  $E_{ad}$  of AB is much higher than that on  $NiWO_4$  surface ( $-1.29 \text{ eV}$  vs.  $-0.91 \text{ eV}$ ). The corresponding structural simulations can be seen in Fig. S6c and S6d. When the heterostructured  $Cu_{0.8}Ni_{0.2}WO_4$  nanoparticles act as catalysts, the adsorption behaviors of  $CH_3OH$  and AB are quite different from those on single  $NiWO_4$  or  $CuWO_4$ .  $E_{ad}$  of  $CH_3OH$  on the Ni site of  $Cu_{0.8}Ni_{0.2}WO_4$  is  $-2.79 \text{ eV}$  while that on the Cu site of  $Cu_{0.8}Ni_{0.2}WO_4$  is only  $-1.83 \text{ eV}$ , demonstrating that  $CH_3OH$

prefers to be adsorbed on the Ni sites of  $Cu_{0.8}Ni_{0.2}WO_4$ . In contrast,  $E_{ad}$  of AB on the Cu surface of  $Cu_{0.8}Ni_{0.2}WO_4$  is  $-2.40 \text{ eV}$  while that on the Ni surface of  $Cu_{0.8}Ni_{0.2}WO_4$  is only  $-1.54 \text{ eV}$ , implying that the Cu sites in  $Cu_{0.8}Ni_{0.2}WO_4$  are inclined to adsorb AB. The structural simulation for the chemisorption behaviors of AB and  $CH_3OH$  molecules on  $Cu_{0.8}Ni_{0.2}WO_4$  interface is illustrated in Fig. 7c–f. Clearly, both the adsorption of  $CH_3OH$  and AB on the  $Cu_{0.8}Ni_{0.2}WO_4$  catalysts is strengthened, well matching the fact that  $\epsilon_d$ -Cu and  $\epsilon_d$ -Ni of  $Cu_{0.8}Ni_{0.2}WO_4$  upshift to Fermi level. Notably,  $Cu_{0.8}Ni_{0.2}WO_4$  catalysts provide two active sites, namely Ni site and Cu sites, accounting for the adsorption and activation of different reactants. The dual active sites can work hand in hand for fast hydrogen release from AB/methanol



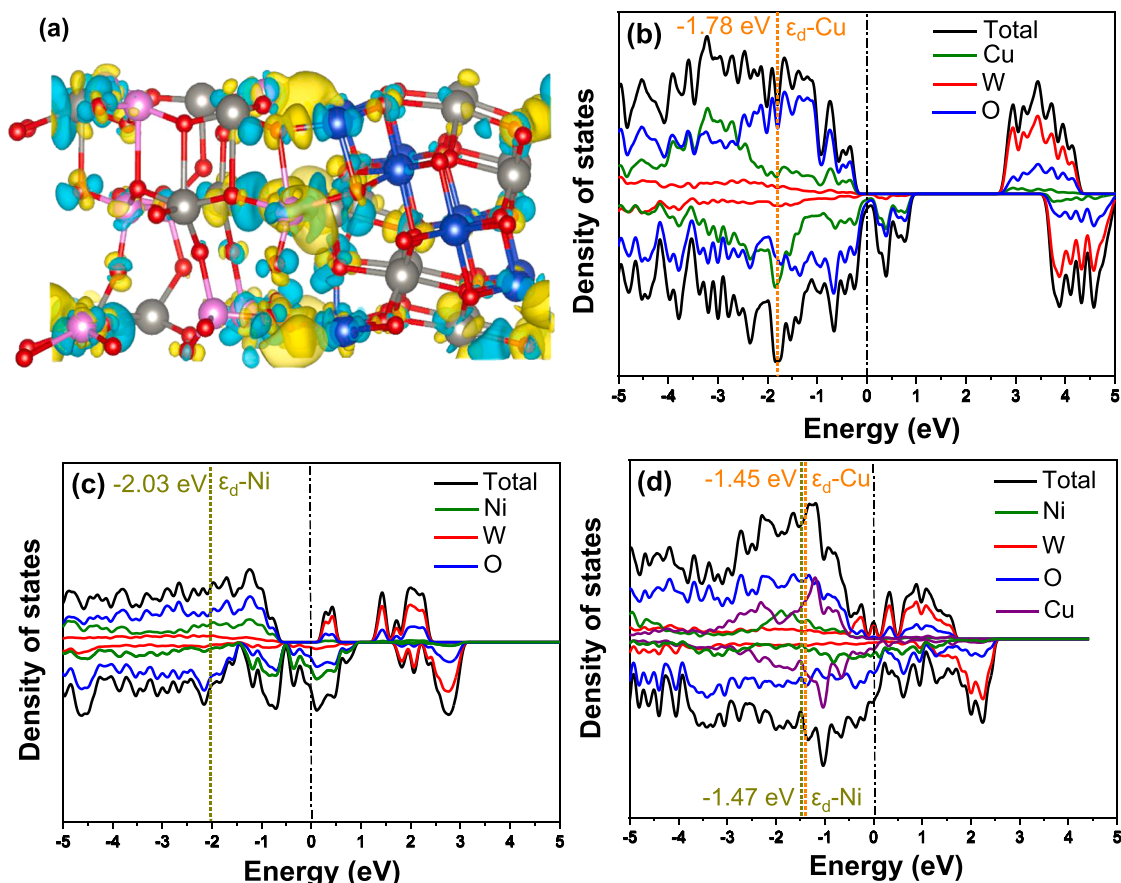
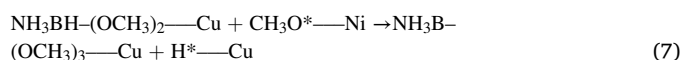
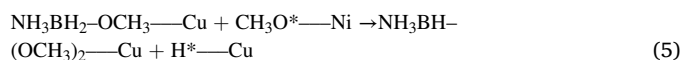
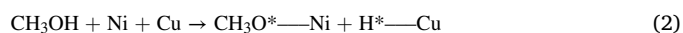


**Fig. 6.** The charge-density difference of  $\text{Cu}_{0.8}\text{Ni}_{0.2}\text{WO}_4$  (a), and DOS of the  $\text{CuWO}_4$  (b),  $\text{NiWO}_4$  (c) and  $\text{Cu}_{0.8}\text{Ni}_{0.2}\text{WO}_4$  (d). The charge accumulation region is rendered in yellow while the charge depletion region is in blue. Color scheme: O, red; Cu, Blue; Ni, Purple; W, Gray.

solution, surpassing the single active site in the methanolysis reaction.

It is known that the mechanisms of AB hydrolysis have been well investigated but a detailed report on the methanolysis mechanisms of AB is scarce in the literature. It has been evidenced that the scission of O-H in water is the rate-determining step (RDS) in AB hydrolysis [42]. The bonding strength of O-H in  $\text{CH}_3\text{OH}$  ( $438.5 \text{ kJ mol}^{-1}$ ) is a little lower than that in water but is high than that of B-N and B-H [51,52]. Thus, the scission of O-H bond of  $\text{CH}_3\text{OH}$  may be involved in RDS. To clarify this, a kinetic isotopic effect (KIE) experiment, in which the  $\text{CH}_3\text{OD}$  instead of  $\text{CH}_3\text{OH}$  was used as a reactant, was carried out to know more about the reaction mechanisms of AB methanolysis. Evidently, the rate of AB methanolysis in  $\text{CH}_3\text{OD}$  is significantly smaller than that in  $\text{CH}_3\text{OH}$  under the same reaction condition, showing a KIE constant of 2.9 (Fig. 8a). The bonds in  $\text{CH}_3\text{OD}$  are almost the same as those of  $\text{CH}_3\text{OH}$  with the exception of O-D bond. The remarkable rate difference implies that the scission of the O-H bond should be RDS in the methanolysis of AB. According to the hydrolysis mechanism of AB [42,53,54] and our experimental results, a suggested methanolysis mechanism of AB is proposed (Fig. 8b): (1) Cu and Ni sites in  $\text{Cu}_{0.8}\text{Ni}_{0.2}\text{WO}_4$  catalysts adsorb AB and methanol, respectively; (2) O-H bond in  $\text{CH}_3\text{O}-\text{H}$  is broken, leading to the formation of  $^*\text{OCH}_3$  and  $\text{H}^*$ ; (3)  $^*\text{OCH}_3$  attacks the B atom of AB, and  $\text{NH}_3\text{BH}_2-\text{OCH}_3$  and another  $\text{H}^*$  are produced; (4) two  $\text{H}^*$  combined together to generate one  $\text{H}_2$  molecule, which will escape from the active sites. Two more  $\text{H}_2$  molecules will be generated via the similar procedure described above. The reaction steps can be expressed as the following:



To further understand the superior catalytic performance of our  $\text{Cu}_{0.8}\text{Ni}_{0.2}\text{WO}_4$  over that of  $\text{CuWO}_4$  and  $\text{NiWO}_4$ , the energy barrier of the RDS in AB methanolysis is investigated by theoretical calculation and the simulation processes are shown in Fig. S7. As can be seen in Fig. 8c, the energy for breaking O-H bond in  $\text{CH}_3\text{OH}$  is 1.03 eV for  $\text{CuWO}_4$ , 0.79 eV for  $\text{NiWO}_4$ , 0.62 eV for the Cu sites of  $\text{Cu}_{0.8}\text{Ni}_{0.2}\text{WO}_4$ , and 0.38 eV for the Ni sites of  $\text{Cu}_{0.8}\text{Ni}_{0.2}\text{WO}_4$ , respectively. Evidently, the energy barriers are relatively large for single  $\text{CuWO}_4$  and  $\text{NiWO}_4$ , accounting for the poor reactivity of  $\text{CuWO}_4$  and  $\text{NiWO}_4$ . When  $\text{CuWO}_4$  and  $\text{NiWO}_4$  are combined together, the charge separation happens on the interface, resulting in the formation of dual active sites in the catalysts, which facilitates the adsorption and activation of reactants. The energy barrier is the smallest when RDS happens on the Ni sites of  $\text{Cu}_{0.8}\text{Ni}_{0.2}\text{WO}_4$ , further demonstrating Ni sites act as the optimal sites for AB methanolysis.

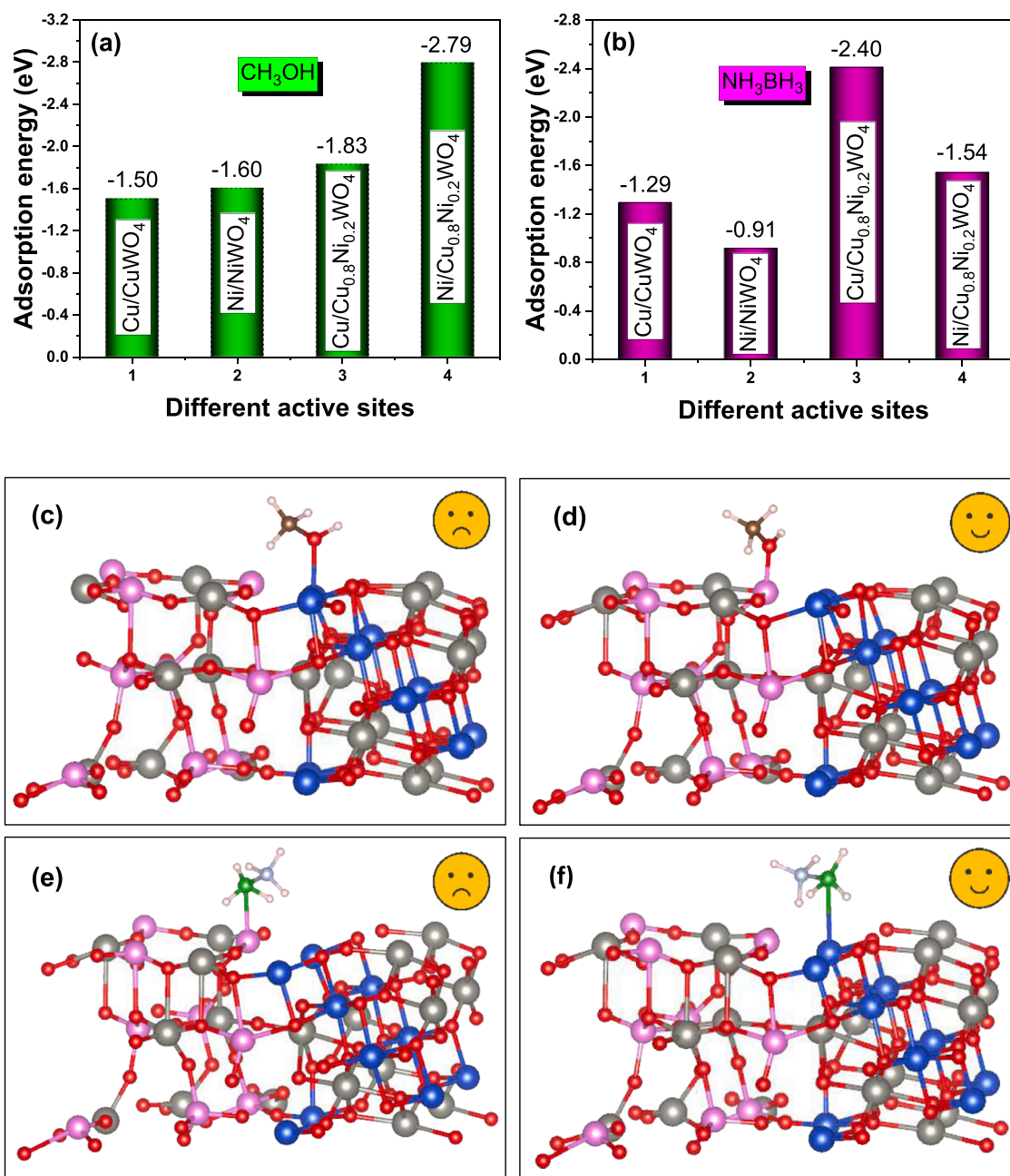


Fig. 7. The adsorption energy of methanol (a) and AB (b), and the structural simulation of adsorption behaviors (c–f) on the different active sites of the Cu<sub>0.8</sub>Ni<sub>0.2</sub>WO<sub>4</sub> catalysts. Color scheme: O, red; Cu, blue; Ni, purple; W, gray; B, green; N, bluish gray; H, silvery.

#### 4. Conclusion

In summary, insoluble tungstates with different components (Cu<sub>x</sub>Ni<sub>1-x</sub>WO<sub>4</sub>,  $x = 0, 0.2, 0.4, 0.6, 0.8$ , and 1) were designed, and their catalytic behaviors in AB methanolysis were systematically studied. It was discovered that the CuWO<sub>4</sub> was active in AB methanolysis, while NiWO<sub>4</sub> was inert during AB methanolysis. By combining NiWO<sub>4</sub> and CuWO<sub>4</sub>, the catalytic performance of the resultant heterojunction could be pronouncedly improved. The heterostructured Cu<sub>0.8</sub>Ni<sub>0.2</sub>WO<sub>4</sub> nanoparticles exhibited a high TOF of 59.0 mol<sub>hydrogen</sub> min<sup>-1</sup> mol<sub>cat</sub><sup>-1</sup> during AB methanolysis, higher than most noble metal-free catalysts in the literature. Investigations into the reaction kinetics verified that AB methanolysis followed zero-order reaction kinetics with respect to AB and pseudo-first-order kinetics with respect to the catalyst. The results of the reusability and stability testing indicated that our

Cu<sub>0.8</sub>Ni<sub>0.2</sub>WO<sub>4</sub> catalyst exhibited good reusability and high stability. Electron transfer between the heterojunction interface of CuWO<sub>4</sub> and NiWO<sub>4</sub> led to the formation of dual active sites, facilitating the adsorption and activation of reactants on the catalyst surface and conducting to fast hydrogen production. The plausible mechanism for AB methanolysis has also been proposed and the scission of O–H bond is the rate-determining step. The findings in this study could serve as guidance for the creation of novel catalysts with excellent performance and low cost in AB methanolysis.

#### CRediT authorship contribution statement

**Jinyun Liao:** Methodology, Formal analysis, Writing – original draft. **Youxiang Shao:** Methodology, Formal analysis, Validation. **Yufa Feng:** Formal analysis. **Jing Zhang:** Formal analysis. **Chunxia Song:** Formal

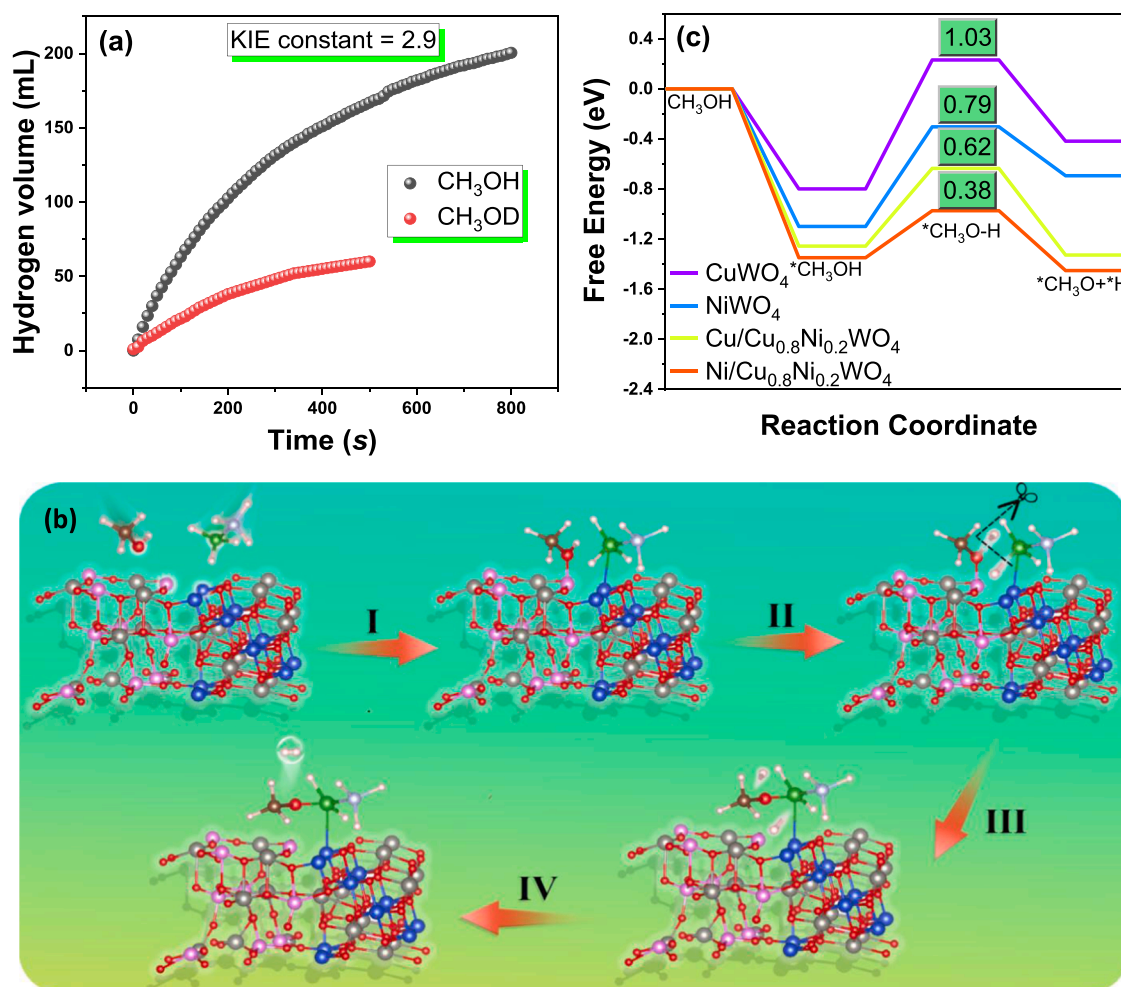


**Fig. 8.** Comparison of hydrogen evolution in the case of CH<sub>3</sub>OH and CH<sub>3</sub>OD as reactants (a); A plausible mechanism of AB methanolysis catalyzed by Cu<sub>0.8</sub>Ni<sub>0.2</sub>WO<sub>4</sub> heterojunction (b); Energy profiles for the RDS (c).

analysis. **Wei Zeng:** Formal analysis. **Jinting Tang:** Formal analysis. **Huafeng Dong:** Validation. **Quanbing Liu:** Validation, Project administration, Funding acquisition. **Hao Li:** Conceptualization, Funding acquisition, Writing – review & editing.

#### Declaration of Competing Interest

The authors declare that they have no known competing financial interests or personal relationships that could have appeared to influence the work reported in this paper.

#### Data Availability

Data will be made available on request.

#### Acknowledgements

This work was supported by the Major and Special Project in the Field of Intelligent Manufacturing of the Universities in Guangdong Province (No. 2020ZDZX2067), the Natural Science Foundation of Huizhou University (Nos. 20180927172750326 and HZU202004), the Key-Area Research and Development Program of Guangdong Province (No. 2020B090919005), and the National Natural Science Foundation of China (Nos. U1801257, 21975056, 52002079).

#### Conflicts of interest

There are no conflicts to declare.

#### Appendix A. Supporting information

Supplementary data associated with this article can be found in the online version at [doi:10.1016/j.apcatb.2022.121973](https://doi.org/10.1016/j.apcatb.2022.121973).

#### References

- [1] Y. He, Y. Peng, Y. Wang, Y. Long, G. Fan, Air-engaged fabrication of nitrogen-doped carbon skeleton as an excellent platform for ultrafine well-dispersed RuNi alloy nanoparticles toward efficient hydrolysis of ammonia borane, *Fuel* 297 (2021), 120750.
- [2] R. Ding, Q. Chen, Q. Luo, L. Zhou, Y. Wang, Y. Zhang, G. Fan, Salt template-assisted in situ construction of Ru nanoclusters and porous carbon: excellent catalysts toward hydrogen evolution, ammonia-borane hydrolysis, and 4-nitrophenol reduction, *Green Chem.* 22 (2020) 835–842.
- [3] J.O. Abe, A.P. Popoola, E. Ajenifuja, O.M. Popoola, Hydrogen energy, economy and storage: review and recommendation, *Int. J. Hydrog. Energy* 44 (2019) 15072–15086.
- [4] W. Wang, Q. Yao, Z.-H. Lu, Bimetallic Ni–Pt nanoparticles immobilized on mesoporous N-doped carbon as a highly efficient catalyst for complete hydrogen evolution from hydrazine borane, *J. Mater. Chem. A* 8 (2020) 13694–13701.
- [5] Q. Luo, Q. Chen, Y. Wang, Y. Long, W. Jiang, G. Fan, Facile, general and environmental-friendly fabrication of O/N-codoped porous carbon as a universal matrix for efficient hydrogen evolution electrocatalysts, *Chem. Eng. J.* 420 (2021), 130483.



- [6] Y. Luo, Q. Yang, W. Nie, Q. Yao, Z. Zhang, Z.-H. Lu, Anchoring IrPdAu nanoparticles on NH<sub>2</sub>-SBA-15 for fast hydrogen production from formic acid at room temperature, *ACS Appl. Mater. Interfaces* 12 (2020) 8082–8090.
- [7] S. Özkır, Transition metal nanoparticle catalysts in releasing hydrogen from the methanolysis of ammonia borane, *Int. J. Hydrog. Energy* 45 (2020) 7881–7891.
- [8] J. Liao, Y. Feng, W. Lin, X. Su, S. Ji, L. Li, W. Zhang, B. Pollet, H. Li, CuO–NiO/Co<sub>3</sub>O<sub>4</sub> hybrid nanoplates as highly active catalyst for ammonia borane hydrolysis, *Int. J. Hydrog. Energy* 45 (2020) 8168–8176.
- [9] Y. Peng, Y. He, Y. Wang, Y. Long, G. Fan, Sustainable one-pot construction of oxygen-rich nitrogen-doped carbon nanosheets stabilized ultrafine Rh nanoparticles for efficient ammonia borane hydrolysis, *J. Colloid Interface Sci.* 594 (2021) 131–140.
- [10] Y. Feng, X. Chen, H. Wang, X. Li, H. Huang, Y. Liu, H. Li, Durable and high performing Ti supported Ni<sub>0.4</sub>Cu<sub>0.6</sub>Co<sub>2</sub>O<sub>4</sub> nanoleaf-like array catalysts for hydrogen production, *Renew. Energy* 169 (2021) 660–669.
- [11] Y. Ge, X. Qin, A. Li, Y. Deng, L. Lin, M. Zhang, Q. Yu, S. Li, M. Peng, Y. Xu, X. Zhao, M. Xu, W. Zhou, S. Yao, D. Ma, Maximizing the synergistic effect of CoNi catalyst on α-MoC for robust hydrogen production, *J. Am. Chem. Soc.* 143 (2021) 628–633.
- [12] Y. Chen, K. Feng, G. Yuan, Z. Kang, J. Zhong, Highly efficient CoNiP nanoboxes on graphene oxide for the hydrolysis of ammonia borane, *Chem. Eng. J.* 428 (2020), 131219.
- [13] X. Su, S. Li, PVP-stabilized Co–Ni nanoparticles as magnetically recyclable catalysts for hydrogen production from methanolysis of ammonia borane, *Int. J. Hydrog. Energy* 46 (2021) 14384–14394.
- [14] C. Yu, J. Fu, M. Muzzio, T. Shen, D. Su, J. Zhu, S. Sun, CuNi nanoparticles assembled on graphene for catalytic methanolysis of ammonia borane and hydrogenation of nitro/nitrile compounds, *Chem. Mater.* 29 (2017) 1413–1418.
- [15] A.K. Figen, Improved catalytic performance of metal oxide catalysts fabricated with electrospinning in ammonia borane methanolysis for hydrogen production, *Int. J. Hydrog. Energy* 44 (2019) 28451–28462.
- [16] M. Yurderi, A. Bulut, I.E. Ertaş, M. Zahmakiran, M. Kaya, Supported copper–copper oxide nanoparticles as active, stable and low-cost catalyst in the methanolysis of ammonia–borane for chemical hydrogen storage, *Appl. Catal. B: Environ.* 165 (2015) 169–175.
- [17] M. Ha, J.-H. Kim, M. You, Q. Li, C. Fan, J.-M. Nam, Multicomponent plasmonic nanoparticles: from heterostructured nanoparticles to colloidal composite nanostructures, *Chem. Rev.* 119 (2019) 12208–12278.
- [18] R.E. Schaak, B.C. Steimle, J.L. Fenton, Made-to-order heterostructured nanoparticle libraries, *Acc. Chem. Res.* 53 (2020) 2558–2568.
- [19] Q.-Q. Chen, Q. Li, C.-C. Hou, C.-J. Wang, C.-Y. Peng, N. López, Y. Chen, Enhancing electrostatic interactions to activate polar molecules: ammonia borane methanolysis on a Cu/Co(OH)<sub>2</sub> nanohybrid, *Catal. Sci. Technol.* 9 (2019) 2828–2835.
- [20] X. Ren, H. Lv, S. Yang, Y. Wang, J. Li, R. Wei, D. Xu, B. Liu, Promoting effect of heterostructured NiO/Ni on Pt nanocatalysts toward catalytic hydrolysis of ammonia borane, *Phys. Chem. Lett.* 10 (2019) 7374–7382.
- [21] Y. Lin, L. Yang, H. Jiang, Y. Zhang, D. Cao, C. Wu, G. Zhang, J. Jiang, L. Song, Boosted reactivity of ammonia borane dehydrogenation over Ni/Ni<sub>2</sub>P heterostructure, *Phys. Chem. Lett.* 10 (2019) 1048–1054.
- [22] H. Wu, Y. Cheng, B. Wang, Y. Wang, M. Wu, W. Li, B. Liu, S. Lu, Carbon dots-confined CoP–CoO nanoheterostructure with strong interfacial synergy triggered the robust hydrogen evolution from ammonia borane, *J. Energy Chem.* 57 (2021) 198–205.
- [23] C. Wang, Y. Ren, J. Zhao, S. Sun, X. Du, M. Wang, G. Ma, H. Yu, L. Li, X. Yu, X. Zhang, Z. Lu, X. Yang, Oxygen vacancy-attired dual-active-sites Cu/Cu<sub>0.76</sub>Co<sub>0.24</sub>O<sub>4</sub> drives electron transfer for efficient ammonia borane dehydrogenation, *Appl. Catal. B: Environ.* 314 (2022), 121494.
- [24] M. Zhou, Z. Liu, X. Li, Z. Liu, Promising three-dimensional flowerlike CuWO<sub>4</sub> photoanode modified with CdS and FeOOH for efficient photoelectrochemical water splitting, *Ind. Eng. Chem. Res.* 57 (2018) 6210–6217.
- [25] A. Bhardwaj, I.H. Kim, L. Mathur, J.Y. Park, S.J. Song, Ultrahigh-sensitive mixed-potential ammonia sensor using dual-functional NiWO<sub>4</sub> electrocatalyst for exhaust environment monitoring, *J. Hazard. Mater.* 403 (2021), 123797.
- [26] V. Balasubramanian, S. Kannan, S.T. Nishanthi, G. Sivakumar, K. Mohanraj, Elucidate the pseudocapacitive behaviour of CuWO<sub>4</sub> electrode synthesized by solid-state reaction, *J. Mater. Sci.: Mater. Electron.* 31 (2020) 10142–10150.
- [27] Y. Feng, H. Wang, X. Chen, F. Lv, Y. Li, Y. Zhu, C. Xu, X. Zhang, H.R. Liu, H. Li, Simple synthesis of Cu<sub>2</sub>O–CoO nanoplates with enhanced catalytic activity for hydrogen production from ammonia borane hydrolysis, *Int. J. Hydrog. Energy* 45 (2020) 17164–17173.
- [28] M.N. Mancheva, R.S. Iordanova, D.G. Klissurski, G.T. Tyuliev, B.N. Kunev, Direct mechanochemical synthesis of nanocrystalline NiWO<sub>4</sub>, *J. Phys. Chem. C* 111 (2007) 1101–1104.
- [29] R. Gupata, B. Boruah, J.M. Modak, G. Madras, Kinetic study of Z-scheme C<sub>3</sub>N<sub>4</sub>/CuWO<sub>4</sub> photocatalyst towards solar light inactivation of mixed populated bacteria, *J. Photochem. Photobiol. A: Chem.* 372 (2019) 108–121.
- [30] F.H. Hsu, S.Y. Hsu, C.W. Pao, J.L. Chen, C.L. Chen, J.M. Chen, K.T. Lu, Electrochemical properties and mechanism of CoMoO<sub>4</sub>@NiWO<sub>4</sub> core-shell nanoplates for high-performance supercapacitor electrode application studied via in situ X-ray absorption spectroscopy, *Nanoscale* 12 (2020) 13388–13397.
- [31] L. Qi, X. Tang, Z. Wang, X. Peng, Pore characterization of different types of coal from coal and gas outburst disaster sites using low temperature nitrogen adsorption approach, *Int. J. Min. Sci. Technol.* 27 (2017) 371–377.
- [32] J. Liao, Y. Feng, X. Zhang, L. Huang, S. Huang, M. Liu, Q. Liu, H. Li, CuO–Co<sub>3</sub>O<sub>4</sub> composite nanoplatelets for hydrolyzing ammonia borane, *ACS Appl. Nano Mater.* 4 (2021) 7640–7649.
- [33] Z.-C. Fu, Y. Xu, S.L.-F. Chan, W.-W. Wang, F. Li, F. Liang, Y. Chen, Z.-S. Lin, W.-F. Fu, C.-M. Che, Highly efficient hydrolysis of ammonia borane by anion (–OH, F, Cl)–tuned interactions between reactant molecules and CoP nanoparticles, *Chem. Commun.* 53 (2017) 705–708.
- [34] C. Peng, C. Hou, Q. Chen, C. Wang, X. Lv, J. Zhong, W. Fu, C. Che, Y. Chen, Cu(OH)<sub>2</sub> supported on Fe(OH)<sub>3</sub> as a synergistic and highly efficient system for the dehydrogenation of ammonia-borane, *Sci. Bull.* 63 (2018) 1583–1590.
- [35] Y. Feng, X. Zhang, Y. Shao, X. Chen, H. Wang, J. Li, M. Wu, H. Dong, Q. Liu, H. Li, Modulating the acidic properties of mesoporous Mo<sub>x</sub>–Ni<sub>0.8</sub>Cu<sub>0.2</sub>O nanowires for enhanced catalytic performance toward the methanolysis of ammonia borane for hydrogen production, *ACS Appl. Mater. Interfaces* 14 (2022) 27979–27993.
- [36] Y. Zheng, W. Bao, G. Liu, S. Qi, D. Yu, K. Ma, Z. Chen, X. Hu, Y. Lou, Cu/Ni–NiO<sub>x</sub> nanoparticles distributed on graphene as catalysts for the methanolysis of ammonia borane to produce hydrogen, *ACS Appl. Nano Mater.* 4 (2021) 14208–14216.
- [37] L. Cui, X. Cao, X. Sun, W. Yang, J. Liu, Host lignin composition affects haustorium induction in the parasitic plants *Phtheirospermum japonicum* and *Striga hermonthica*, *ChemCatChem* 10 (2018) 710–715.
- [38] D. Özhava, N. Kılıçaslan, S. Özkır, PVP-stabilized nickel(0) nanoparticles as catalyst in hydrogen generation from the methanolysis of hydrazine borane or ammonia borane, *Appl. Catal. B: Environ.* 162 (2015) 573–582.
- [39] Q. Yao, M. Huang, Z.-H. Lu, Y. Yang, Y. Zhang, X. Chen, Z. Yang, Methanolysis of ammonia borane by shape-controlled mesoporous copper nanostructures for hydrogen generation, *Dalton Trans.* 44 (2015) 1070–1076.
- [40] B. Mo, S. Li, H. Wen, H. Zhang, H. Zhang, J. Wu, B. Li, H. Hou, Functional group regulated Ni/Ti<sub>3</sub>C<sub>2</sub>T<sub>x</sub> (T<sub>x</sub> = F, –OH) holding bimolecular activation tunnel for enhanced ammonia borane hydrolysis, *ACS Appl. Mater. Interfaces* 14 (2022) 16320–16329.
- [41] C.C. Hou, Q. Li, C.J. Wang, C.Y. Peng, Q.Q. Chen, H.F. Ye, W.F. Fu, C.M. Che, N. López, Y. Chen, Ternary Ni–Co–P nanoparticles as noble-metal-free catalysts to boost the hydrolytic dehydrogenation of ammonia-borane, *Energy Environ. Sci.* 10 (2017) 1770–1776.
- [42] Y. Feng, Y. Shao, X. Chen, Y. Zhang, Q. Liu, M. He, H. Li, Sea-urchin-like hollow CuMoO<sub>4</sub>–CoMoO<sub>4</sub> hybrid microspheres, a noble-metal-like robust catalyst for the fast hydrogen production from ammonia borane, *ACS Appl. Energy Mater.* 4 (2021) 633–642.
- [43] World Health Organization, International Standards for Drinking Water, WHO, Geneva, 1071.
- [44] J. Liao, D. Lu, G. Diao, X. Zhang, M. Zhao, H. Li, Co<sub>0.8</sub>Cu<sub>0.2</sub>MoO<sub>4</sub> microspheres composed of nanoplatelets as a robust catalyst for the hydrolysis of ammonia borane, *ACS Sustain. Chem. Eng.* 6 (2018) 5843–5851.
- [45] D. Lu, J. Liao, H. Li, S. Ji, B.G. Pollet, Co<sub>3</sub>O<sub>4</sub>/CuMoO<sub>4</sub> hybrid microflowers composed of nanorods with rich particle boundaries as a highly active catalyst for ammonia borane hydrolysis, *ACS Sustain. Chem. Eng.* 7 (2019) 16474–16482.
- [46] C.-C. Hou, Q. Li, C.-J. Wang, C.-Y. Peng, Q.-Q. Chen, H.-F. Ye, W.-F. Fu, C.-M. Che, N. López, Y. Chen, Ternary Ni–Co–P nanoparticles as noble-metal-free catalysts to boost the hydrolytic dehydrogenation of ammonia-borane, *Energy Environ. Sci.* 10 (2017) 1770–1776.
- [47] W. Chen, J. Ji, X. Feng, X. Duan, G. Qian, P. Li, X. Zhou, D. Chen, W. Yuan, Mechanistic insight into size-dependent activity and durability in Pt/CNT catalyzed hydrolytic dehydrogenation of ammonia borane, *J. Am. Chem. Soc.* 136 (2014) 16736–16739.
- [48] B. Qiu, C. Wang, N. Zhang, L. Cai, Y. Xiong, Y. Chai, CeO<sub>2</sub>-induced interfacial Co<sup>2+</sup> octahedral sites and oxygen vacancies for water oxidation, *ACS Catal.* 9 (2019) 6484–6490.
- [49] N. Acerbi, S.C.E. Tsang, G. Jones, S. Golunski, P. Collier, Rationalization of interactions in precious metal/ceria catalysts using the d-band center model, *Angew. Chem.* 125 (2013) 7891–7895.
- [50] N. Wang, S. Ning, X. Yu, D. Chen, Z. Li, J. Xu, H. Meng, D. Zhao, L. Li, Q. Liu, B. Lu, S. Chen, Graphene composites with Ru–RuO<sub>2</sub> heterostructures: highly efficient Mott–Schottky-type electrocatalysts for pH-universal water splitting and flexible zinc–air batteries, *Appl. Catal. B: Environ.* 302 (2022), 120838.
- [51] D.F. McMillen, D.M. Golden, Hydrocarbon bond dissociation energies, *Ann. Rev. Phys. Chem.* 33 (1982) 493–532.
- [52] F. Tong, X. Liang, M. Liu, Z. Wang, Y. Liu, P. Wang, H. Cheng, Y. Dai, Z. Zheng, B. Huang, Plasmon-enhanced water activation for hydrogen evolution from ammonia-borane studied at a single-particle level, *ACS Catal.* 12 (2022) 3558–3565.
- [53] X. Huang, Y. Liu, H. Wen, R. Shen, S. Mehd, X. Wu, E. Liang, X. Guo, B. Li, Ensemble-boosting effect of Ru–Cu alloy on catalytic activity towards hydrogen evolution in ammonia borane hydrolysis, *Appl. Catal. B: Environ.* 287 (2021), 119960.
- [54] H. Zhang, Y. Liu, H. Wei, C. Wang, T. Liu, X. Wu, S. Ashraf, S. Mehd, S. Guan, Y. Fan, X. Yue, B. Liu, Y. Zhang, H. Cao, B. Li, Atomic-bridge structure in B–Co–P dual-active sites on boron nitride nanosheets for catalytic hydrogen generation, *Appl. Catal. B: Environ.* 314 (2022), 121495.